Physics of Fluids

On the generalized Beltramian motion of the bidirectional vortex in a right-cylindrical cyclone with a hollow core

Cite as: Phys. Fluids **34**, 043603 (2022); https://doi.org/10.1063/5.0087621
Submitted: 07 February 2022 • Accepted: 15 March 2022 • Published Online: 07 April 2022

Orie M. Cecil and Joseph Majdalani

Physics of Fluids ARTICLE scitation.org/journal/phf

On the generalized Beltramian motion of the bidirectional vortex in a right-cylindrical cyclone with a hollow core

Cite as: Phys. Fluids **34**, 043603 (2022); doi: 10.1063/5.0087621
Submitted: 7 February 2022 · Accepted: 15 March 2022 ·
Published Online: 7 April 2022

Orie M. Cecil[a] and Joseph Majdalani[b]

AFFILIATIONS

Department of Aerospace Engineering, Auburn University, 211 Davis Hall, Auburn, Alabama 36849-5338, USA

Note: This paper is part of the special topic, Centennial of the Kármán-Pohlhausen Momentum-Integral Approach.
[a]**Electronic mail:** orie.cecil@gmail.com
[b]**Author to whom correspondence should be addressed:** joe.majdalani@gmail.com

ABSTRACT

In this work, an exact inviscid solution is developed for the incompressible Euler equations in the context of a bidirectional, cyclonic flowfield in a right-cylindrical chamber with a hollow core. The presence of a hollow core confines the flow domain to an annular swirling region that extends into a toroid in three-dimensional space. The procedure that we follow is based on the Bragg–Hawthorne framework and a judicious assortment of boundary conditions that correspond to a wall-bounded cyclonic motion with a cylindrical core. At the outset, a self-similar stream function is obtained directly from the Bragg–Hawthorne equation under the premises of steady, axisymmetric, and inviscid conditions. The resulting formulation enables us to describe the bidirectional evolution of the so-called inner and outer vortex motions, including their fundamental properties, such as the interfacial layer known as the mantle; it also unravels compact analytical expressions for the velocity, pressure, and vorticity fields, with particular attention being devoted to their peak values and spatial excursions that accompany successive expansions of the core radius. By way of confirmation, it is shown that removal of the hollow core restores the well-established solution for a fully flowing cylindrical cyclone. Immediate applications of cyclonic flows include liquid and hybrid rocket engines, swirl-driven combustion devices, as well as a multitude of heat exchangers, centrifuges, cyclone separators, and flow separation devices that offer distinct advantages over conventional, non-swirling systems.

I. INTRODUCTION

Cyclonic flows manifest themselves over a wide range of spatial and temporal scales that extend from astrophysical motions to laboratory-induced helical patterns. Among various atmospheric events, swirling storm systems can be observed in meteorological phenomena such as tornadoes, dust devils, typhoons, hurricanes, and tropical cyclones, if only to name a few. These naturally occurring cyclonic events remain predominantly unconfined and either unidirectional or bipolar, as opposed to swirling flows reproduced in a laboratory, which occasionally appear in a bounded, bidirectional setting. Furthermore, laboratory-induced vortices have been shown to possess distinct advantages over traditional flows in several technological applications, and these range from industrial cyclone separators to propulsive devices, such as the Vortex Injection Hybrid Rocket Engine (VIHRE) conceived by Knuth *et al.*[1] and the Vortex Combustion Cold-Wall (VCCW) engine developed by Chiaverini *et al.*[2]

In fact, the list of so-called vortex-fired combustion devices extends to a multitude of technological concepts. These include, but are not limited to, the Vortex Combustion Ramjet,[3] the Vortex Combustion Combined Cycle (VCCC) engine,[4] the Cool-Wall Vortex Combustion Chamber (CWVCC),[5–7] the MAELSTROM-G25 thruster,[8] and the VR-3A Vision Engine, which have been chiefly developed by Chiaverini and co-workers at Orbital Technologies Corporation (ORBITEC™).[9–11] Over time, these concepts have gradually evolved into a volumetrically efficient spheroidal model intended for upper stage propulsive applications by Sierra Space Corporation. More specifically, they have paved the way for the development of a compact, convectively film-cooled and highly efficient VR35K-A VORTEX® engine; the latter is characterized by wall-tangential

injection and the presence of a cyclonic flowfield that resembles the internal motion of cyclone separators.[12–14]

From a practical standpoint, the advantages that accompany swirl-induced motions have been leveraged to modulate bluff body flow separation, which is often encountered in combustion chambers.[15,16] In this context, the so-called Trapped Vortex Combustor has been shown to be highly effective at improving flame stability, reducing pressure losses, and controlling the emission characteristics of gas turbine engines. Examples include the Step-Swirl Gas-Turbine Combustor by Durbin *et al.*,[17] the Trapped Vortex Combustor by Katta and Roquemore,[18] the Plasma-Assisted Tornado Combustor by Matveev,[19] the Triple Vortex Combustor by Matveev *et al.*,[20] and the Hybrid Solar Receiver Combustor (HSRC) by Long *et al.*[21]

In both hydrocyclones and VIHRE-VCCW engine concepts, the bidirectional motion is produced by two co-rotating and counter-flowing streams that are driven by a tangentially injected fluid. The incoming stream spirals around and sweeps the outer wall in one axial direction before bouncing off the apex of the cavity, reversing direction, and returning through the inner vortex region at a faster angular speed.

Among the multiple uses of a bidirectional vortex configuration, cyclone separators stand apart among the most ubiquitous. The corresponding cylindrically or conically shaped containers are frequently relied upon in the mineral and petrochemical processing industries to separate particles of varying sizes and densities. For example, in oil refinery plants, large cyclonic separators provide an attractive alternative to the use of heavy-duty filters for gas–oil extraction. In catalytic cracking, they can be helpful at accelerating the segregation of catalytic particles from reacting gaseous mixtures. In cement processing, they can be employed as integral components of kiln preheating and, in sawmills, they may serve to eliminate sawdust from extracted air. They may be similarly employed to separate greasy deposits caused by prolonged air ventilation in exhaust fume hoods.

In wastewater and sewage treatment plants, a hydrocyclone may be effectively used to separate solid waste from water. To accomplish this, the sediment-laden water is typically swirled toward the bottom of the container, where, by virtue of gravity and inertia, denser particles are removed from the mixture and collected at what is referred to as the "spigot." The lighter sediment and remaining water are then siphoned back through the low pressure core region in an upward spiral that is channeled through what is often dubbed the "vortex finder."

What is most relevant to the present investigation is, perhaps, the development of an air core within the inner vortex region, which is a characteristic feature of many hydrocyclones. According to Gupta *et al.*,[22] the presence of a low pressure region along the central axis of fluid rotation often leads to the suction of air into the chamber at the base or apex, where an opening is invariably used to dispose of the heavy underflow. The introduction of air into the inner vortex can naturally result in the institution of a hollow core that persists along the entire length of the vortex chamber. In actuality, Neesse and Dueck[23] suggest that even with a sealed apex, an air core can still develop because of the inevitable trace amounts of air that may be entrained in the feed system. Due to the low pressure condition along the axis of the chamber, the air may then coalesce into bubbles which, when collected along the center of the unit, give rise to a hollow core. This behavior is further confirmed through non-reactive gaseous simulations of right-cylindrical cyclonic chambers with various outlet sizes and curvatures.[24] Therein, the development of a re-entrant backflow region that begins at the outlet section and then creeps into the chamber has been verified computationally and attributed to a combination of geometric characteristics and outflow properties.[24] It has also been validated experimentally by Khan.[25]

From a practical standpoint, the inception of a hollow core can drastically influence the separation efficiency of hydrocyclones as well as the flow patterns that accompany the resulting steady-state motion. The need to elucidate the relations that exist between the core diameter, flow development, and separation efficiency has, in fact, spurred on several theoretical studies of mainly non-reactive fluid mixtures. According to the approach taken by Davidson,[26] an iterative analytical formulation for the air core radius may be provided in terms of the axial and tangential velocities, thus permitting the user to maximize the volume flow rate through the chamber outlet for a fixed pressure head. This study also recognizes that the core diameter must be determined through either experimentation or computation, or else treated as a variable parameter that may be left unspecified during the course of the investigation. Then, based on a numerical simulation approach by Evans *et al.*,[27] it has been shown that the separation efficiency may be improved by altogether prohibiting the air core from developing, and that air core prevention may be achieved by inserting a solid rod into the core region. Another air core suppression technique by Luo *et al.*[28] consists of sealing the apex with water. However, although these techniques may be effective in certain types of cyclone separators, they are unlikely to remain viable in the context of a swirl-driven rocket chamber. For this reason, the emergence of a hollow core, along with its impact on flow properties, continue to represent a fundamentally unexplored area of investigation for the VCCW and VIHRE configurations.

While analytical models of bidirectional vortices with hollow cores remain fairly limited, some noteworthy research has been conducted on the bidirectional motion in fully flowing conical and cylindrical chambers. A few examples include the work by Ying and Chang,[29] Bloor and Ingham,[30] as well as Davidson,[31] and those by Alekseenko *et al.*,[32,33] Concha,[34] Cortes and Gil,[35] Shtern and Borissov,[36] and Barber and Majdalani,[10] namely, where the salient features of the flow are described in both cylindrical and conical chamber configurations. One may also find relevant the work of Battaglia *et al.*[37] on external fire whirls, and those by Vyas and Majdalani[38] and Majdalani,[11] who come across fundamentally different classes of inviscid Trkalian, Beltramian, and essentially complex-lamellar cyclonic motions in cylindrical chambers. At the time of this writing, the search for theoretical models of wall-bounded cyclonic motions continues as reflected in the Beltramian and basically complex-lamellar profiles developed for hemispherical chamber configurations.[12–14]

The present investigation continues to tread the same line of research inquiry into the character of wall-bounded cyclonic fields in cylindrical configurations by focusing on the implications of a uniformly distributed hollow or solid core. Unlike other formulations that have appeared in the literature, our derivation will be initiated from the axisymmetric Bragg–Hawthorne equation (BHE) in a frictionless environment; the underlying assumptions will enable us to specify the total pressure head and angular momentum relations at the forefront of the analysis. Then using a judicious choice of boundary conditions, a closed-form analytical solution will be obtained whence the formerly constructed model

by Vyas and Majdalani[38] will be identically restored by simply suppressing its core radius. We also note that throughout this work, the inner core radius will be treated as a variable parameter in order to investigate the connection between the size of the hollow core and the principal flow attributes.

II. PROBLEM FORMULATION

A. Geometry and flow conditions

The geometric configuration under investigation consists of a right-cylindrical chamber of length L, an inner core radius of c, and an outer radius of a, as illustrated in Fig. 1(a). In the case of a rigid inner core boundary, such as a tubular insert, the annular region bounded between $\bar{r} = c$ and a forms either a rectangular or square toroid, depending on the proportions between $(a - c)$ and L. As usual, the use of cylindrical polar coordinates, $(\bar{r}, \theta, \bar{z})$, which are anchored at the base of the chamber, helps to define spatial orientations. In order to mimic the presence of a nozzle attachment or a vortex finder, a single outlet with a radius of b is positioned at $\bar{z} = L$. In this setup, the working fluid is directed into the chamber just upstream of the outlet and tangentially to the sidewall (at $\bar{r} = a$) with an average velocity of U. Owing to the intense centrifugal pressure forces that this motion engenders, the flow is compelled to spiral around the annulus and traverse the length of the chamber twice before exiting. The ensuing bipolar motion gives rise to two well-demarcated zones that are separated by a spinning interfacial layer called "mantle." The bidirectional nature of this motion may be attributed to its incorporation of an outer vortex loop between $\bar{r} = a$ and the mantle, with a negative axial velocity (spinning toward $\bar{z} = 0$), and an inner vortex loop between $\bar{r} = c$ and the mantle, with a positive axial velocity (spinning toward $\bar{z} = L$). In this configuration, the flow reverses axial direction while approaching the headwall at $\bar{z} = 0$. For further clarity, a three-dimensional sketch of the solution domain and coordinate system is provided in Fig. 1(a) along with a three-dimensional rendering of the annular domain and labeled regions in Fig. 1(b).

B. Fluid dynamic equations and assumptions

Essential to this study is the steady, axisymmetric, inviscid, and incompressible relation coined by different authors as the Squire–Long, the Long–Squire, and, more commonly perhaps, the Bragg–Hawthorne equation (BHE).[39–41] Despite its rare mention in mainstream fluid mechanics textbooks,[42–45] the BHE framework has been shown to be surprisingly effective at disclosing useful approximations for helical flows in a variety of phenomenological applications.[9–14] In its most basic form, the BHE framework assumes steady, isentropic, and axisymmetric conditions, where the total pressure head $\bar{H}$ as well as the tangential angular momentum $\bar{B}$ become sole functions of the stream function $\bar{\psi}$, with $2\pi\bar{B}$ representing the circulation. This simplification facilitates the selection of suitable relations for $\bar{B}$ and $\bar{H}$ that enable the user to transform the problem into a tractable partial differential equation. More specifically, in a polar-cylindrical reference frame, the Bragg–Hawthorne equation can be expressed, as shown in detail by Hicks[46] or White and Majdalani,[45] using

$$\frac{\partial^2\bar{\psi}}{\partial\bar{r}^2} - \frac{1}{\bar{r}}\frac{\partial\bar{\psi}}{\partial\bar{r}} + \frac{\partial^2\bar{\psi}}{\partial\bar{z}^2} = \bar{r}^2\frac{\mathrm{d}\bar{H}}{\mathrm{d}\bar{\psi}} - \bar{B}\frac{\mathrm{d}\bar{B}}{\mathrm{d}\bar{\psi}}. \tag{1}$$

In seeking a solution for Eq. (1), one may recognize that, under the stated assumptions, the angular momentum is conserved; one may also use a form for the stagnation head that results in a linear equation that is identical to that obtained by Vyas and Majdalani.[38] As such, $\bar{B}$ and $\bar{H}$ can be selected in accordance with

$$\bar{B}(\bar{\psi}) = B_0 = aU, \quad \frac{\mathrm{d}\bar{B}}{\mathrm{d}\bar{\psi}} = 0, \tag{2}$$

$$\bar{H}(\bar{\psi}) = H_0 - \frac{1}{2}H_1^2\bar{\psi}^2, \quad \frac{\mathrm{d}\bar{H}}{\mathrm{d}\bar{\psi}} = -H_1^2\bar{\psi}, \tag{3}$$

where B_0, H_0, and H_1 refer to pure constants. We recall that U denotes the tangential injection velocity over a finite area A_i near the $\bar{z} = L$ endwall section. In the absence of friction, this value at the injection

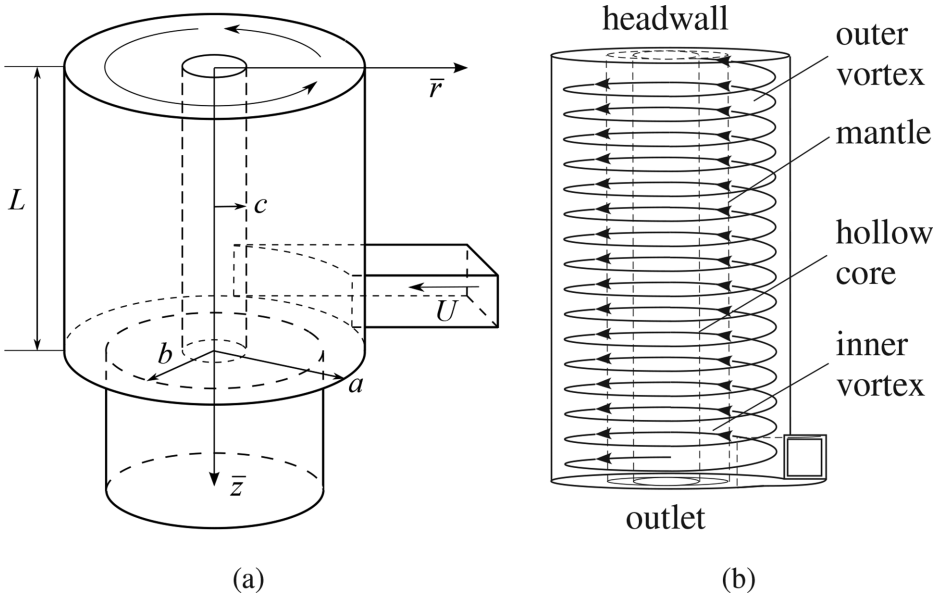

FIG. 1. We show (a) the coordinate system and basic geometric parameters as well as (b) the corresponding labeled regions of a cylindrically-cyclonic motion that is constrained between an inner core radius c and an outer wall at a.

site persists along the length of the chamber; the corresponding mass flow rate can be integrated over a finite inlet area as defined by Eq. (6) of Sec. II C. Furthermore, the conditions associated with Eqs. (2) and (3) result in the same governing partial differential equation for the stream function used by Culick,[47] specifically

$$\frac{\partial^2\bar{\psi}}{\partial\bar{r}^2}-\frac{1}{\bar{r}}\frac{\partial\bar{\psi}}{\partial\bar{r}}+\frac{\partial^2\bar{\psi}}{\partial\bar{z}^2}+H_1^2\bar{r}^2\bar{\psi}=0. \tag{4}$$

Interestingly, the much cited Taylor–Culick flow profile for simplified, right-cylindrical, internally burning solid rocket motors may be recovered from Eq. (4) as a special case.[47]

C. Boundary conditions

The boundary conditions may be taken to fundamentally mirror those prescribed in the context of a bidirectional vortex with no hollow core.[38] This can be accomplished by retaining most conditions except for those that apply at the core. By moving the constraints that are formerly enforced at the centerline to a finite radius c, the resulting set of requirements translates into

(a) no axial flow at the headwall or fore-end closure: $\bar{u}_z(\bar{r},0)=0$;
(b) a vanishing radial velocity at the inner core boundary: $\bar{u}_r(c,\bar{z})=0$;
(c) a vanishing radial velocity at the outer sidewall boundary: $\bar{u}_r(a,\bar{z})=0$;
(d) a mass balance between the incoming and outgoing flow rates: $2\pi\int_c^b \bar{u}_z(a,L)\bar{r}\,\mathrm{d}\bar{r}=UA_i=\bar{Q}_i$.

Here, $\bar{Q}_i$ represents an inlet volume flow rate prescribed by the tangential injection velocity U over a finite inlet area A_i as discussed previously. This parameter captures the sensitivity of the model to changes in mass inflow. In the interest of simplicity, the foregoing conditions may be further rearranged and conveniently expressed in terms of the stream function by putting

$$\left.\frac{1}{\bar{r}}\frac{\partial\bar{\psi}}{\partial\bar{r}}\right|_{(\bar{r},0)}=0,\quad \left.\frac{1}{\bar{r}}\frac{\partial\bar{\psi}}{\partial\bar{z}}\right|_{(c,0)}=0,\quad \left.\frac{1}{\bar{r}}\frac{\partial\bar{\psi}}{\partial\bar{z}}\right|_{(a,0)}=0, \tag{5}$$

$$\text{and}\quad \int_c^b \left.\frac{1}{\bar{r}}\frac{\partial\bar{\psi}}{\partial\bar{r}}\right|_{(\bar{r},L)}\bar{r}\,\mathrm{d}\bar{r}=\frac{UA_i}{2\pi}. \tag{6}$$

Now that the problem is fully defined, one can proceed to extract a solution for Eq. (4) that stands in compliance with Eqs. (5) and (6).

III. AN EXACT EULER SOLUTION

A. Stream function

In view of the linearity of Eq. (4), one may substitute the separable form $\bar{\psi}(\bar{r},\bar{z})=f(\bar{r})g(\bar{z})$ and collect,

$$\frac{1}{f(\bar{r})}\left[f''(\bar{r})-\frac{1}{\bar{r}}f'(\bar{r})+H_1^2\bar{r}^2f(\bar{r})\right]=-\frac{\ddot{g}(\bar{z})}{g(\bar{z})}=\begin{cases}0 & (\text{type 0}),\\ +\nu^2 & (\text{type I}),\\ -\nu^2 & (\text{type II}),\end{cases} \tag{7}$$

where primes and dots imply differentiation with respect to $\bar{r}$ and $\bar{z}$, respectively. For the remainder of this analysis, our attention will be focused on the type 0 case because it corresponds to the simplest partial solution that can be made to satisfy the physical requirements associated with the model at hand; we get

$$\bar{\psi}=(k_1\bar{z}+k_2)\left[k_3\sin\left(\frac{1}{2}H_1\bar{r}^2\right)+k_4\cos\left(\frac{1}{2}H_1\bar{r}^2\right)\right]. \tag{8}$$

At this stage, the boundary conditions in Eqs. (5) and (6) may be directly applied. Beginning with a vanishing axial flow at $\bar{z}=0$, we obtain

$$k_2H_1\left[k_3\cos\left(\frac{1}{2}H_1\bar{r}^2\right)-k_4\sin\left(\frac{1}{2}H_1\bar{r}^2\right)\right]=0,\quad \forall\bar{r}. \tag{9}$$

Here, $H_1=0$ leads to the trivial outcome of a zero axial velocity throughout the chamber; instead, $k_2=0$ must be chosen for the condition to hold at any radial location. Next, we may ensure that no flow crosses the inner core boundary, be it a streamline or an impermeable surface, by requiring that

$$k_1\left[k_3\sin\left(\frac{1}{2}H_1c^2\right)+k_4\cos\left(\frac{1}{2}H_1c^2\right)\right]=0. \tag{10}$$

With $k_2=0$, the use of $k_1=0$ must be avoided lest a trivial solution is precipitated in the form of $\bar{\psi}=0$. The alternative is to specify k_4 using

$$k_4=-k_3\tan\left(\frac{1}{2}H_1c^2\right). \tag{11}$$

To make further headway, one may substitute Eq. (11) into Eq. (8) and evaluate the radial velocity at $\bar{r}=a$ in such a manner as to secure the impermeable sidewall condition. This operation leaves us with

$$H_1=\frac{2n\pi}{a^2-c^2}, \tag{12}$$

where n controls the number of flow reversals and, therefore, internal mantles.[14,48,49] Since the subject of multiple mantles falls outside the scope of this study, we restrict the present analysis to a single, internal flow reversal by taking $n=1$. The corresponding stream function becomes

$$\bar{\psi}=\bar{\psi}_0\bar{z}\left[\sin\left(\frac{\pi\bar{r}^2}{a^2-c^2}\right)-\tan\left(\frac{\pi c^2}{a^2-c^2}\right)\cos\left(\frac{\pi\bar{r}^2}{a^2-c^2}\right)\right]. \tag{13}$$

Note that the lumped constant $\bar{\psi}_0\equiv k_1k_3$ may be deduced from the mass balance relation in Eq. (6). By equating the outflow to the inflow, one recovers

$$\bar{\psi}_0=\frac{UA_i}{2\pi L}\csc\left[\frac{\pi(b^2-c^2)}{a^2-c^2}\right]\cos\left(\frac{\pi c^2}{a^2-c^2}\right). \tag{14}$$

This enables us to consolidate all pertinent terms and write

$$\bar{\psi}=\frac{UA_i}{2\pi L}\bar{z}\csc\left[\frac{\pi(b^2-c^2)}{a^2-c^2}\right]\cos\left(\frac{\pi\bar{r}^2}{a^2-c^2}\right)\cos\left(\frac{\pi c^2}{a^2-c^2}\right)\times\left[\tan\left(\frac{\pi\bar{r}^2}{a^2-c^2}\right)-\tan\left(\frac{\pi c^2}{a^2-c^2}\right)\right]. \tag{15}$$

B. Normalization

Through the process of normalization, not only will the expression for the stream function in Eq. (15) be significantly reduced, but the main geometric and physical group parameters in

this problem will be unraveled as well. Here, we use the sidewall radius a and the tangential inlet velocity U as reference values to normalize all of the remaining variables. We take

$$r=\frac{\bar{r}}{a},\quad z=\frac{\bar{z}}{a},\quad l=\frac{L}{a},\quad \beta=\frac{b}{a},\quad \alpha=\frac{c}{a},\quad B=\frac{\bar{B}}{Ua}, \tag{16}$$

$$u_r=\frac{\bar{u}_r}{U},\quad u_z=\frac{\bar{u}_z}{U},\quad u_\theta=\frac{\bar{u}_\theta}{U},\quad \psi=\frac{\bar{\psi}}{Ua^2},\quad \text{and}\quad Q_i=\frac{\bar{Q}_i}{Ua^2}=\frac{A_i}{a^2}=\frac{1}{\sigma}. \tag{17}$$

Following these substitutions, Eq. (15) collapses into

$$\psi=\kappa z\frac{\sin\left[\eta(r^2-\alpha^2)\right]}{\sin\left[\eta(\beta^2-\alpha^2)\right]},\quad \eta\equiv\frac{\pi}{1-\alpha^2},\quad \kappa\equiv\frac{1}{2\pi\sigma l}, \tag{18}$$

where the modified swirl number $\sigma=a^2/A_i$ and inflow parameter κ, which are discussed in detail by Vyas and Majdalani,[38] resurface naturally. The corresponding velocities become

$$u_r=-\frac{1}{r}\frac{\partial\psi}{\partial z}=-\frac{1}{r}\kappa\csc\left[\eta\left(\beta^2-\alpha^2\right)\right]\sin\left[\eta\left(r^2-\alpha^2\right)\right], \tag{19}$$

$$u_\theta=\frac{B}{r}=\frac{1}{r}, \tag{20}$$

and

$$u_z=\frac{1}{r}\frac{\partial\psi}{\partial r}=2z\eta\kappa\csc\left[\eta\left(\beta^2-\alpha^2\right)\right]\cos\left[\eta\left(r^2-\alpha^2\right)\right]. \tag{21}$$

By way of verification, it may be seen that the special case of an infinitesimal core radius of $c=0$, which corresponds to the limiting configuration of a right-cylindrical chamber with no hollow core, may be readily recovered by setting $\alpha=0$. One obtains

$$\mathbf{u}=-\frac{\kappa}{r}\frac{\sin(\pi r^2)}{\sin(\pi\beta^2)}\mathbf{e}_r+\frac{1}{r}\mathbf{e}_\theta+2\pi\kappa z\frac{\cos(\pi r^2)}{\cos(\pi\beta^2)}\mathbf{e}_z, \tag{22}$$

which matches, as it should, the profile by Vyas and Majdalani.[38]

IV. RESULTS AND DISCUSSION

To better understand the behavior of the mean flow solution, it is helpful to characterize its fundamental features. These begin with the mantle position and velocity field, both of which vary with the core diameter and chamber aspect ratio. Additionally, the streamlines associated with this motion will be useful to visualize, along with both pressure and vorticity fields. In this process, the peak or absolute extrema of each of these flow variables will be identified and evaluated whenever possible.

A. Mantle location

The term mantle (or spinning wheel) refers to the interfacial layer that stands between the so-called updraft and downdraft, to use cyclonic flow terminology. Along this interface, the axial velocity is compelled to vanish as the flow switches polarity while moving radially inwardly from the outer, annular vortex, to the inner, core vortex. As such, mantle development in right-cylindrical chambers may be viewed as a distinguishing property of all bidirectional motions. Under incompressible conditions, theoretical analyses predict an axially invariant mantle location that is defined by $r=\beta^*$ at $u_z=0$. For example, Vyas and Majdalani[38] find a mantle at $\beta^*=0.707$ for a mean flow profile with no hollow core. In a higher energy demanding flowfield of the Beltramian type, the mantle shifts inwardly to $\beta^*=0.628$.[11] The duality of these mantle positions seems to be connected to the type of motion that develops, be it a generalized Beltramian profile satisfying $\nabla\times\boldsymbol{\omega}\times\mathbf{u}=0$, or a strictly Beltramian field observing $\boldsymbol{\omega}\times\mathbf{u}=0$. In fact, the theoretical predictions of approximately 0.63 and 0.71 match quite favorably the classical experimental findings of 0.62 and 0.72 reported by Smith.[50,51]

By setting $r=\beta^*$ and suppressing the axial velocity in Eq. (21), the theoretical location of the mantle may be deduced from

$$2z\eta\kappa\csc\left[\eta\left(\beta^2-\alpha^2\right)\right]\cos\left[\eta\left(\beta^{*2}-\alpha^2\right)\right]=0. \tag{23}$$

Equation (23) may be solved straightforwardly for β^* as a function of $\alpha=c/a$; one gets

$$\beta^*=\sqrt{\frac{1+\alpha^2}{2}}\approx 0.707\sqrt{1+\alpha^2}. \tag{24}$$

In what follows, Fig. 2(a) will be used to illustrate the sensitivity of the mantle to variations in α. Although the plot covers the entire range of $0\le\alpha<1$, practical values of α seldom exceed 0.4. Evidently, $\alpha=0$ leads to the initial mantle value of $1/\sqrt{2}$, which reproduces its counterpart in a cyclonic chamber with no hollow core.[38] Furthermore, a shifted radial coordinate x may be introduced in the form of

$$x=\frac{\bar{r}-c}{a-c}=\frac{r-\alpha}{1-\alpha}, \tag{25}$$

where x represents a rescaled radius relative to the width of the annulus, i.e., the radial fraction at a given position relative to the usable width of the annular region. This fraction, in turn, enables us to specify precisely at the mantle location, $x^*=(\beta^*-\alpha)/(1-\alpha)$, as the net width of the inner vortex region relative to the width of the annulus. As illustrated in Fig. 2(b), x^* varies from 0.707 at $\alpha=0$ to a theoretical $x^*=0.5$ at the impractical value of $\alpha\to 1$. In this fictitious configuration, the inner and outer radial fractions become evenly split as the hollow core is extended over the entire radius, thus reducing the annulus to an infinitesimally thin segment (or line) at the sidewall. In practice, however, as long as $0\le\alpha\le 0.4$, the inner vortex segment will remain thicker than its outer counterpart, with $0.6026\le x^*\le 0.7071$. Moreover, it may be readily shown that areas occupied by the inner and outer vortex regions in an r-θ plane remain equal, $\forall\alpha$, with the dimensional areas being expressible by

$$A_{\text{inner}}=A_{\text{outer}}=\frac{1}{2}\pi a^2(1-\alpha^2). \tag{26}$$

Interestingly, this equal sharing of inner and outer flow areas proves to be another basic property of this motion.

B. Helical velocity vector field

To mitigate unnecessary collisions in the exit plane,[38] the open fraction at the base can be equated to the mantle radius. This arrangement leads to a smooth outflow as the inner vortex courses its way out of the chamber through its main opening at $z=l$. To avoid undesirable flow obstructions at the outlet, β will be equated to the mantle radius

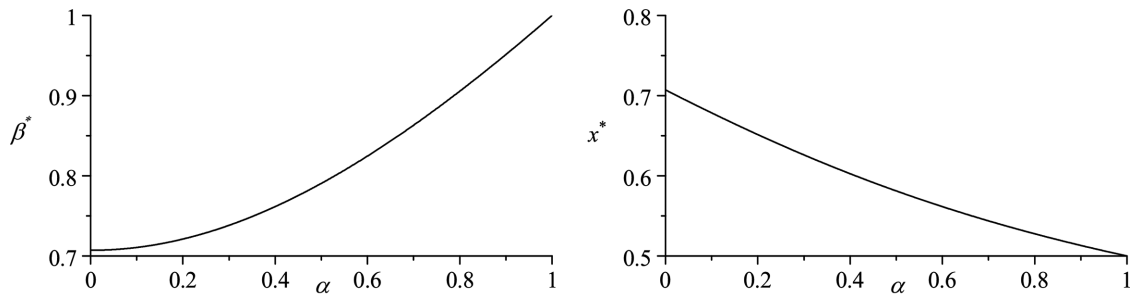

(a) Mantle location (b) Net radial fraction of the inner vortex

FIG. 2. Sensitivity of (a) the mantle location and (b) the net annular fraction of the inner vortex to variations in the dimensionless core radius α.

β^* for the remainder of this study. In fact, the process of substituting Eq. (24) into Eq. (21) reduces the radial and axial velocities to the compact expressions

$$u_r = -\frac{1}{r}\kappa \sin\left[\eta(r^2-\alpha^2)\right] \quad \text{and} \quad u_z = 2\eta\kappa z \cos\left[\eta(r^2-\alpha^2)\right]. \tag{27}$$

1. Axial velocity distribution

We begin by exploring the behavior of the axial velocity through the radial distribution of an axially invariant form of Eq. (27) in Fig. 3(a). This is accomplished by first renormalizing u_z with κz and then plotting the resulting expression over the chamber radius at four evenly spaced values of α, namely, $\alpha = 0$, 0.25, 0.5, and 0.75. The turning nature of the flow is captured in Fig. 3(a), where each u_z curve is seen to switch polarity by crossing the mantle-defining horizontal axis at a value that is consistent with Eq. (24). It should be noted that, by virtue of the inviscid nature of the foregoing analysis (which is required to produce an exact solution), the no-slip conditions at both the inner and outer chamber boundaries are relaxed. In the presence of viscosity, one expects the axial velocity to dip sharply at either extremity to the extent of vanishing eventually both at $r = \alpha$ (in the case of a solid inner wall) and $r = 1$ at the sidewall. Conversely, for the strictly inviscid case, the peak axial velocity, which occurs at either boundary (positive at $r = \alpha$ and negative at $r = 1$), may be determined from $(u_z)_{\max} = 2\eta\kappa z$. Along similar lines, to isolate the effect of an expanding core radius on the peak axial velocity, $(u_z)_{\max}$ is renormalized by κz and written as function of α, viz.,

$$\frac{(u_z)_{\max}}{\kappa z} = \frac{2\pi}{1-\alpha^2}, \quad \alpha \in [0, 1). \tag{28}$$

This expression for the axially invariant peak velocity in the streamwise direction is illustrated in Fig. 3(b), where Eq. (28) may be seen to vary from a minimum value of 6.283 in the case of $\alpha = 0$, to 7.480 at $\alpha = 0.4$. As the annular segment is further narrowed, the axial speed is quickly accelerated to permit the transport of the same amount of fluid through a narrower passage. This explains the superlative value of 33.069, which is reached at $\alpha = 0.9$ along with the unbounded growth that accompanies $\alpha \to 1$, as the annular flow area is compressed into a line. The gradual increase in $(u_z)_{\max}$ with increasing α can also be inferred from Fig. 3(a).

2. Radial velocity distribution

The radial velocity given by Eq. (27) may be seen to be axially invariant. As such, it may be fully characterized in Fig. 4 by capturing its radial variation at four equispaced values of α along with the variation of its peak magnitude as the core radius is increased from 0 to 1.

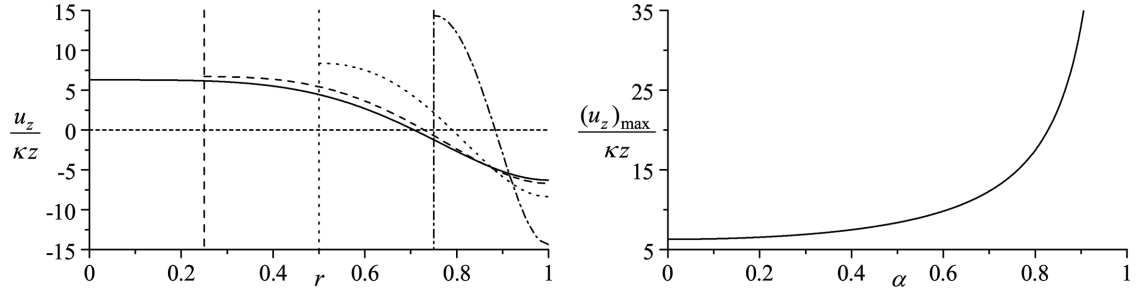

(a) (b)

FIG. 3. Renormalized axial velocity distribution versus (a) r for $\alpha = 0$ (——), 0.25 (– – –), 0.5 (·····), and 0.75 (— · —) along with (b) its peak value at the edge of the hollow core for $\alpha \in [0, 1)$.

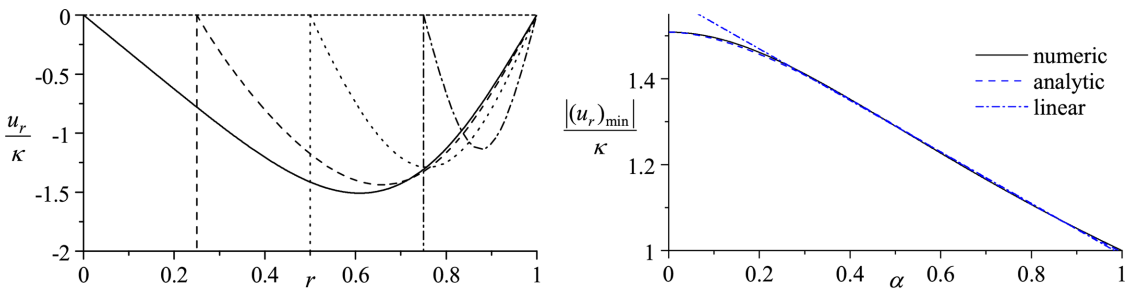

FIG. 4. Renormalized radial velocity distribution versus (a) r for $\alpha = 0$ (——), 0.25 (– – –), 0.5 (·····), and 0.75 (— · —) along with (b) its peak value within the annular segment for $\alpha \in [0, 1)$.

In contrast to the behavior of u_z, the peak radial velocity decreases with successive increases in α. This may be attributed to the diminished usable space between the core radius and the sidewall, which forces the axial velocity to increase while simultaneously suppressing the intensity of the radial motion. Moreover, this behavior can be visualized in Fig. 4(b), where numerical and two approximate solutions are shown (see the Appendix for more details). For values of α greater than 0.3, a linear approximation proves sufficient. Practically, the location of the peak radial velocity $r_{\min}$ may be determined from the vanishing radial gradient of u_r. By differentiating u_r with respect to r and setting the result equal to zero, one obtains

$$2\pi r_{\min}^2 - (1-\alpha^2)\tan\left[\eta(r_{\min}^2 - \alpha^2)\right] = 0. \tag{29}$$

The sensitivity of $r_{\min}$ to α is illustrated in Fig. 5(a) side-by-side with $x_{\min}$ in Fig. 5(b), where the net fraction of the annulus at the point of maximum absolute u_r is displayed. In both Figs. 5(a) and 5(b), the numerical result is shown along with the analytical and linear approximations using dashed and chained lines, respectively (see the Appendix). In comparison to the mantle character, the peak radial velocity occurs at $r_{\min} = x_{\min} = 0.6091$ in the case of $\alpha = 0$; it shifts to $x_{\min} = 0.5255$ at $\alpha = 0.4$, and then asymptotes to the same mantle locus of 0.5 when the width of the annulus is shrunk according to $\alpha \to 1$.

3. Crossflow velocity

In addition to the peak $(u_r)_{\min}$, which occurs at $r_{\min}$, another bidirectional flow property consists of the crossflow velocity, which may be evaluated at $r = \beta^*$. Physically, $(u_r)_{\text{cross}}$ denotes the speed at which fluid transport takes place from the outer annulus to the inner vortex along the length of the mantle. For the generalized Beltramian profile developed here, the radial crossflow proves to be a simple constant that may be readily determined from

$$(u_r)_{\text{cross}} = -\kappa\sqrt{\frac{2}{1+\alpha^2}} = -\frac{\kappa}{\beta^*}. \tag{30}$$

It can thus be seen that larger values of $(u_r)_{\text{cross}}$ occur when β^* and, in turn, α diminish, with the maximum crossflow being realized in the case of $\alpha = 0$. Furthermore, $(u_r)_{\text{cross}}$ increases with successive increases in κ, namely, when the magnitude of the swirl velocity is reduced relative to its axial and radial counterparts. According to Eq. (18), such a condition is approached when (σl), the product of the swirl number and the chamber aspect ratio is reduced. Finally, since $(u_r)_{\text{cross}}$ represents the sole mechanism by which mass may be transferred from the outer vortex to the inner region, a simple integration along the length of the mantle may be used to verify that mass conservation is secured. This can be accomplished by first evaluating and confirming that

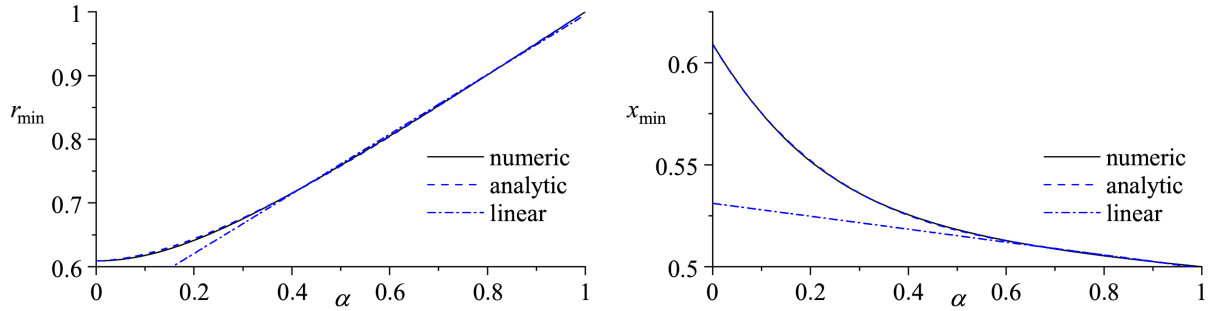

FIG. 5. Spatial variation of (a) the peak radial velocity locus and (b) corresponding usable chamber width fraction for $\alpha \in [0, 1)$.

$$2\pi\beta^* \int_0^l |u_r(\beta^*, z)| \mathrm{d}z = 2\pi\kappa l = Q_i. \tag{31}$$

Clearly, the integration of the distributed mass flow rate across the mantle interface, which extends over the entire chamber length, reproduces the flow entering the domain at $z = l$. In other words, all mass entering the chamber at the base of the cyclonic chamber must cross the mantle at some point.

4. Tangential velocity distribution

Finally, the tangential velocity component given by Eq. (20) proves to be identical to the result obtained by Vyas and Majdalani,[38] which is developed in the absence of a hollow core. However, since $r \in [\alpha, 1]$, u_θ remains finite except for the case of $\alpha = 0$. In view of the inviscid assumption, u_θ does not vanish at the inner core boundary, sidewall, or headwall. In this case, accounting for viscous effects will be required to capture the no-slip condition in the azimuthal direction at the headwall, as well as the inner and outer walls.

C. Vector field and corresponding streamlines

In order to better visualize the evolving cyclonic flowfield, streamlines that capture the bidirectionality of the motion are provided in Fig. 6 using a representative value of $\alpha = 0.25$ and six decreasing chamber aspect ratios. Using r-z planar slices and an off-swirl inflow parameter of $\kappa = 1$, results are shown in Figs. 6(a)–6(f) over a range of non-dimensional chamber lengths corresponding to $l = 3, 2, 1, 0.75, 0.5$, and 0.25. Although a unit value of κ is used, these two-dimensional vector lines remain rather universal. They may be shown to be independent of the off-swirl parameter because both u_r and u_z, whose relative proportion controls the behavior of the solution in the r-z plane, are equally multiplied by κ. Besides the vector fields, which clearly display the radially inward flow across the mantle interface (chained lines), we also depict the boundaries of the hollow core (broken lines), whose presence becomes further accentuated with successive decreases in l. Interestingly, one recovers in Fig. 6(d) the case of a square-shaped toroid; this situation occurs because the non-dimensional usable radius at $\alpha = 0.25$, which is evaluated simply from $(a - c)/a = 0.75$, matches the non-dimensional chamber height of $l = 0.75$. In fact, a square-shaped toroid may be realized anytime $1 - \alpha = l$, such as in the obvious case of $\alpha = 0.5$ and $l = 0.5$.

To further explore the sensitivity of the solution to variations in the hollow core fraction, vector lines corresponding to six equispaced values of α are provided in Fig. 7. These may be viewed as being representative of the streamline curvatures for $\alpha = 0, 0.1, 0.2, 0.3, 0.4$, and 0.5, irrespective of κ. Also shown are the inner core and mantle interfaces, with the latter being given by Eq. (24). Accordingly, the radius of the mantle may be seen to shift radially outwardly with successive expansions of the inner core radius. In fact, it may be readily confirmed that the chained line shifts closer to the middle of the usable flow domain within the annular region as α is further incremented. Based on Eq. (25), one can track the mantle fraction within the flow annulus using

$$x^* = \frac{\sqrt{(\alpha^2+1)/2} - \alpha}{1-\alpha} = \frac{1}{\sqrt{2}} + \left(\frac{1}{\sqrt{2}} - 1\right)\alpha + \left(\frac{3}{2\sqrt{2}} - 1\right)\alpha^2 + O(\alpha^3), \tag{32}$$

where the Maclaurin series expansion restores the well-known mantle fraction of $1/\sqrt{2}$ in the absence of a hollow core. This limiting case is reflected in Fig. 7(a), which depicts the quasi complex-lamellar profile given by Eq. (22). Conversely, a Taylor series expansion of x^* that assumes a large inner core fraction returns

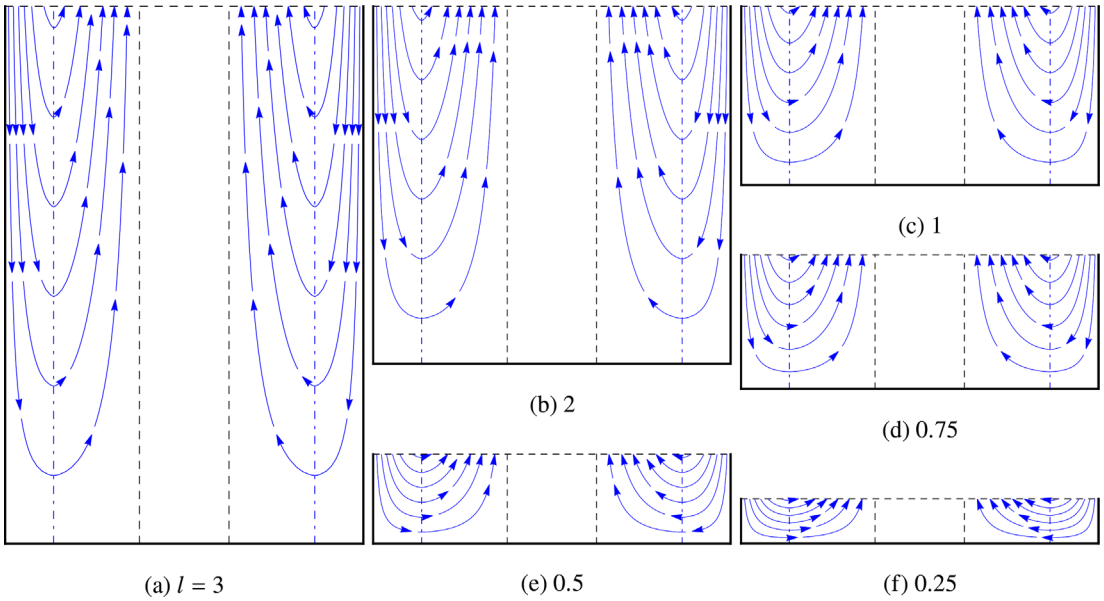

FIG. 6. Side views of the generalized Beltramian streamlines for six different chamber aspect ratios corresponding to (a) $l = 3$, (b) 2, (c) 1, (d) 0.75, (e) 0.5, and (f) 0.25. The broken and chained lines represent the flow domain and mantle boundaries, respectively. These are taken for $\alpha = 0.25$, $\alpha < r \leq 1$, and $0 \leq z \leq l$.

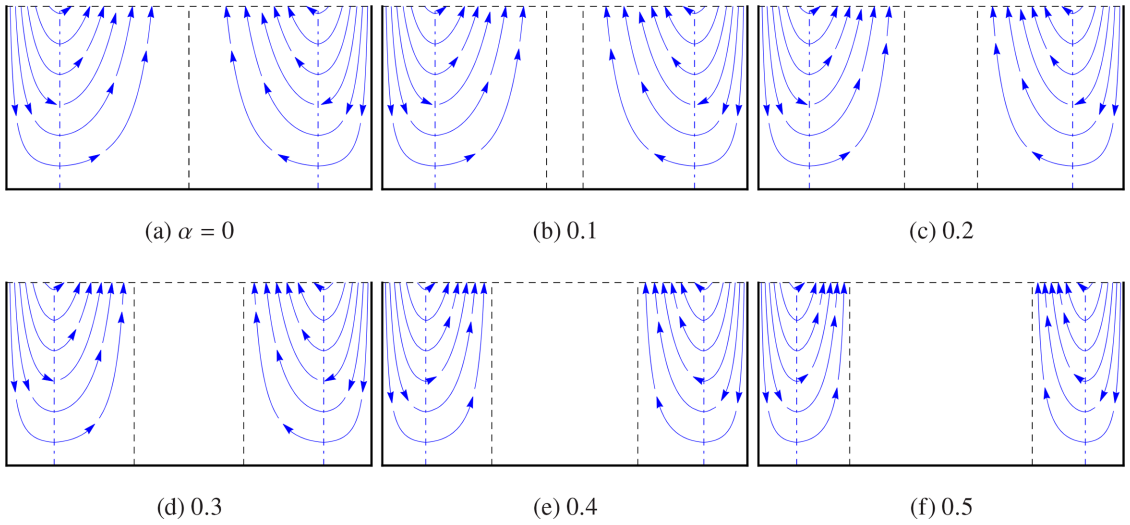

FIG. 7. Side views of the generalized Beltramian streamlines for six equispaced chamber core fractions corresponding to (a) $\alpha = 0$, (b) 0.1, (c) 0.2, (d) 0.3, (e) 0.4, and (f) 0.5. The broken and chained lines represent the flow domain and mantle boundaries, respectively. These are taken for $l = 1$, $\alpha < r \leq 1$, and $0 \leq z \leq l$.

$$x^* = \frac{1}{2} - \frac{\alpha - 1}{8} + \frac{1}{16}(\alpha - 1)^2 + O\left[(\alpha - 1)^3\right]. \tag{33}$$

Equation (33) helps to ascertain that $x^* \to 1/2$ for the infeasible case of $\alpha \to 1$, which renders the cyclonic motion impossible to develop. One is practically drawn to this condition even at $\alpha = 0.5$ in Fig. 7(f), where $\beta^* = 0.7906$ and $x^* = 0.5811$. Although the midpoint fraction is not yet reached, further expansions of the inner core radius continue to reposition the mantle interface such that a nearly even split of the annular segment is eventually achieved between the inner and outer vortex regions. For example, the use of $\alpha = 0.8$ leads to $\beta^* = 0.9055$ and $x^* = 0.5277$.

Having explored the behavior of the vector field in the r-z plane, it may be helpful at this point to shift attention to the swirling character of the solution. This may be accomplished in Fig. 8 using polar slices at different values of κ. Due to the underlying axisymmetry, one way to realize the r-θ motion is to envision superimposing the tangential angular speed associated with u_θ in a manner that causes the planar streamlines described in Figs. 6 and 7 to revolve around the chamber's axis of rotation.

Noting that the streamline patterns in the r-θ plane are prescribed by the relative contributions of u_r and u_θ, and recalling that these remain, in turn, controlled by their proportionality constant κ, the latter becomes a key characteristic parameter. In fact, its bearing on the swirling vector field may be readily inferred from Fig. 8; therein, the solution is visualized using a fixed core radius of $\alpha = 25\%$ and four successive values of $\kappa = 1, 2, 5$, and 10 that span one order of magnitude between Figs. 8(a) and 8(d). Also shown is the mantle intersection with the polar plane (chained line), which demarcates the inner and outer swirling regions.

Based on these graphs, several observations can be made. First, as the off-swirl parameter κ is incremented, it may be realized that the magnitudes of u_r and u_z increase in relation to u_θ. As a result, the vector lines become progressively more reflective of the inward radial transport, with markedly diminished swirling attributes, except near the centerline. This may be ascribed to the fact that, as $r \to 0$, the free vortex form of u_θ will rapidly overtake the motion by eclipsing the values of u_r and u_z, irrespective of κ. This behavior is perhaps to be expected in the absence of viscous corrections that typically give rise to

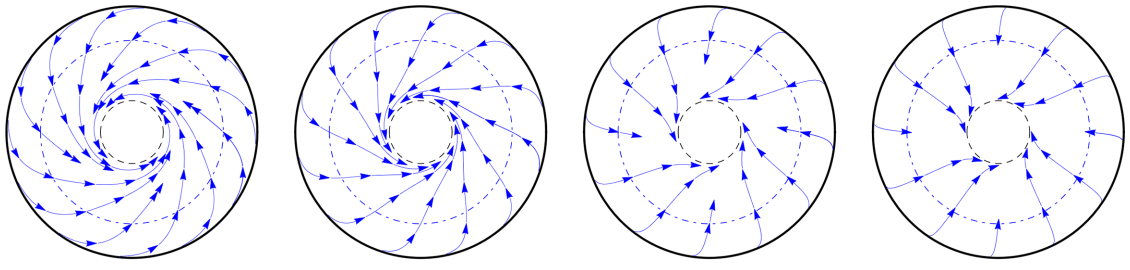

FIG. 8. Top views of the generalized Beltramian streamlines in a horizontal r-θ plane for $\alpha = 25\%$, $l = 1$, and an off-swirl parameter of (a) $\kappa = 1$, (b) 2, (c) 5, and (d) 10. The broken and chained lines represent the inner core and mantle lines, respectively.

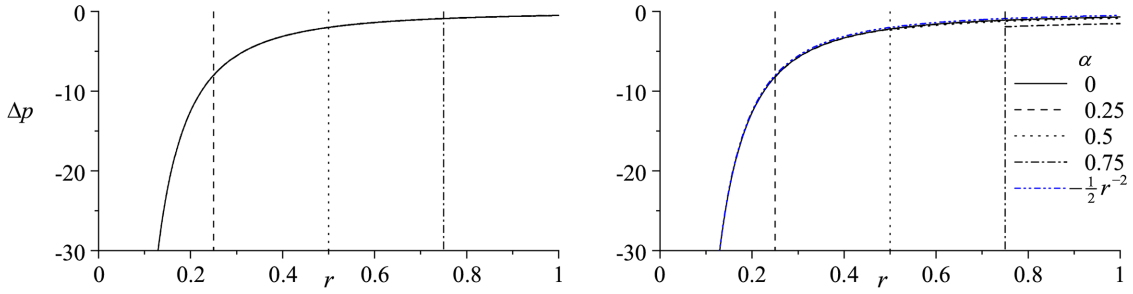

(a) $z = 0$ (b) $z = 5$

FIG. 9. Pressure drop at (a) $z = 0$ (headwall) and (b) $z = 5$ using four characteristic values of α and $\kappa = 0.2$.

a forced vortex motion in the vicinity of the centerline. Because of the precipitous rise of u_θ near the chamber axis, a bathtub vortex may be seen to develop as $r \to 0$ for all values of κ. In contrast, when κ is increased, a vector field that is progressively more dominated by radial transport may be seen to evolve as the sidewall is approached.

D. Pressure distribution

The pressure distribution can be recovered from the dimensionless conservation of momentum equation. One gets

$$\frac{\partial p}{\partial r} = \frac{1}{r^3}\{1 + \kappa^2(\sin^2[\eta(r^2 - \alpha^2)] - \eta r^2 \sin[2\eta(r^2 - \alpha^2)])\}$$

and

$$\frac{\partial p}{\partial z} = 4\eta^2\kappa^2 z. \tag{34}$$

At this juncture, partial integration can be used to retrieve

$$\Delta p = -\frac{1}{2r^2}\left\{1 + \frac{1}{2}\kappa^2\left(8\eta^2 z^2 r^2 + 1 - \cos\left[2\eta(r^2 - \alpha^2)\right]\right)\right\}, \tag{35}$$

where $\Delta p = p - p_0$ may be confirmed to be strongly influenced by the leading-order term, $-1/(2r^2)$, notwithstanding the core expansion radius or z. The resulting behavior may be further inferred from the radial evolution of the pressure drop, which is illustrated in Fig. 9 both at $z = 0$ and $z = 5$. This is accomplished using a relatively large value of $\kappa = 0.2$. By comparing Fig. 9(a) and Fig. 9(b), the differences between the pressure drops taken at four distinct values of α may be perceived as being insignificant. The quasi-frozen behavior of Δp may be traced back to Eq. (35), where α appears in the term multiplying κ^2, and which happens to be too small to retain in most practical applications. The role of κ may thus be viewed as that of offsetting the effect of core expansion on the headwall pressure that accompanies successive increases in α. This canceling effect remains true for an appreciable distance down the bore and only begins to diverge for large aspect ratios with $l \geq 5$. Interestingly, so long as $\alpha > 0$, Δp will reach a finite value at the inner boundary because of the hollow core.

In similar fashion, the radial and axial pressure gradients are showcased in Fig. 10. As with the pressure distribution in Fig. 9, the radial gradient can be approximated by $\partial p/\partial r \approx 1/r^3$ for practical values of κ and α. This proves once more to be virtually insensitive to the inner core radius α, axial station z, and inflow parameter κ, unless these values become fairly large. In order to exaggerate the effects of a changing inner core radius and thus artificially magnify imperceptible deviations graphically, an unusually large value of $\kappa = 1$ is employed in Fig. 10(a). Consequently, some deviations are observed as α is

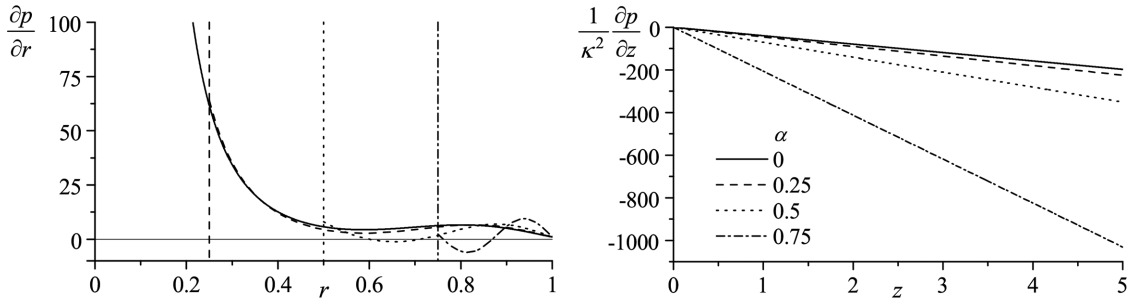

(a) Radial pressure gradient (b) Axial pressure gradient

FIG. 10. Variations of the normalized radial and axial pressure gradients with respect to (a) radial and (b) axial coordinates using four characteristic values of $\alpha = 0, 0.25, 0.5,$ and 0.75.

incremented from 0 to 1. Finally, when attention is turned to the axial pressure gradient in Fig. 10(b), a dependence on the inner core radius α may be observed along with a linear variation of the pressure drop in the streamwise direction irrespectively of the radial location. Such behavior may be corroborated by the corresponding relation in Eq. (34).

E. Vorticity distribution

The mean flow vorticity may be readily calculated from $\boldsymbol{\omega} = \nabla \times \mathbf{u}$ which, for the generalized Beltramian model, leaves us with a single non-vanishing term; we get

$$\omega_r = \omega_z = 0 \quad \text{and} \quad \omega_\theta = 4\eta^2 \kappa r z \sin\left[\eta(r^2 - \alpha^2)\right]. \tag{36}$$

The evolution of the vorticity may be surmised from Fig. 11(a), where $\omega = \omega_\theta$ is first renormalized by κz to make it axially invariant and then showcased at four equispaced values of α. Based on this graph, a maximum can be seen to occur between $r = \alpha$ and 1, with a skewness toward the sidewall at the outskirt of the mantle. To better characterize the radial location of $(\omega_\theta)_{\max}$, its locus $\tilde{r}_{\max}$ may be retrieved from

$$\sin\left[\eta(\tilde{r}_{\max}^2 - \alpha^2)\right] + 2\eta \tilde{r}_{\max}^2 \cos\left[\eta(\tilde{r}_{\max}^2 - \alpha^2)\right] = 0. \tag{37}$$

The root of Eq. (37) may be readily computed and presented in Fig. 11(b), where the shifting of $\tilde{r}_{\max}$ and, correspondingly, the fraction of the usable width $\tilde{x}_{\max}$, are depicted as functions of α. Here, $\tilde{x}_{\max}$ starts at a value of 0.7646, which exceeds the mantle location of 0.7071; it then decreases rather linearly to a value of 0.6619 at $\alpha = 0.4$, where the mantle shifts to 0.6026; finally, it asymptotes to a value of unity at the sidewall. Conversely, the annular fraction $\tilde{x}_{\max}$ that accompanies $(u_r)_{\max}$ diminishes rapidly from 0.609 to 0.5255 at $\alpha = 0.4$ and continues nonlinearly to a value of 0.5 as $\alpha \to 1$. We recall that the latter corresponds to a limiting singular case for which the hollow core will occupy the entire chamber to the extent of preventing any cyclonic motion from forming.

Besides a numerical outcome for Eq. (37), a closed-form asymptotic expression for $\tilde{r}_{\max}$ may be constructed. This may be accomplished by first identifying the basic leading-order solution that corresponds to $\alpha = 0$, specifically

$$\sin X^{(0)} + 2X^{(0)} \cos X^{(0)} = 0, \quad X \equiv \pi \tilde{r}_{\max}^2. \tag{38}$$

This simple form enables us to confirm that $\tilde{r}_{\max}^{(0)} \approx 0.764\,596$. In this vein, using the method of successive approximations, the root's dependence on α may be captured by letting

$$X(\alpha) = X^{(0)} + g(\alpha) X^{(1)} + \cdots, \tag{39}$$

where $X^{(0)} \approx 1.836\,597\,2$. Finally, assuming $g(\alpha) = \alpha^{-2}$ and substituting Eq. (39) into Eq. (37), one retrieves, for $0 < \alpha < 0.5$,

$$X^{(1)} = \frac{1}{4B}\left\{2\cot A - 2\alpha^2 B X^{(0)} + \alpha^2 B \cot A - \alpha^4 B \cot A + \alpha^2 \csc A \right. \\ \left. \times \sqrt{\frac{8B \sin A\left[2X^{(0)} \cos A + \sin A - \alpha^2 \sin A\right]}{\alpha^2} + \left[\left(\frac{2}{\alpha^2} + B - B\alpha^2\right)\cos A - 2BX^{(0)} \sin A\right]^2}\right\} \tag{40}$$

with

$$A = \frac{X^{(0)} - \pi\alpha^2}{1 - \alpha^2} \quad \text{and} \quad B = \frac{1}{\alpha^2(1 - \alpha^2)}. \tag{41}$$

A visual comparison of the asymptotic approximation, $\tilde{r}_{\max} = \sqrt{X(\alpha)/\pi}$, and its corresponding $\tilde{x}_{\max}$ are displayed in Fig. 11(b) along with the numerically obtained values over a practical range of α. These show excellent agreement up to $\alpha \approx 0.5$.

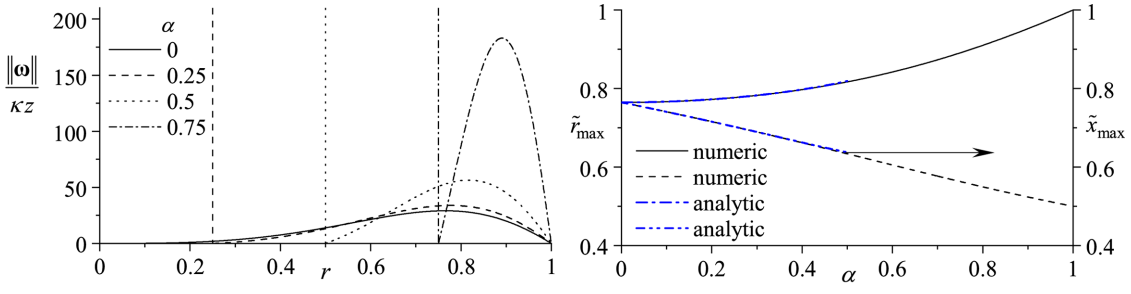

(a) Vorticity (b) Radial location of maximum vorticity

FIG. 11. Renormalized vorticity distribution in the radial direction using (a) four characteristic values of α and including (b) the sensitivity of vorticity's peak location to wide variations in $0 \le \alpha < 1$.

At this juncture, with the vorticity in hand, the Lamb vector, $\ell = \boldsymbol{\omega} \times \mathbf{u}$, may be evaluated and expressed as

$$\ell = 8\eta^3 rz^2\kappa^2 \csc\left[\eta(\beta^2-\alpha^2)\right] \cos\left[\eta(r^2-\alpha^2)\right] \sin\left[\eta(r^2-\alpha^2)\right]\mathbf{e}_r + 4\eta^2 z\kappa^2 \csc\left[\eta(\beta^2-\alpha^2)\right] \sin^2\left[\eta(r^2-\alpha^2)\right]\mathbf{e}_z. \quad (42)$$

Based on Eq. (42), it may be readily verified that $\nabla \times \ell = 0$, thus confirming the generalized Beltramian character of this motion. Along similar lines, the helicity density, $\mathcal{H}$, which denotes the inner product of the velocity and vorticity vectors,[52] may be determined from

$$\mathcal{H} = \mathbf{u} \cdot \boldsymbol{\omega} = 4\eta^2 \kappa z \sin\left[\eta(r^2-\alpha^2)\right]. \quad (43)$$

Interestingly, the helicity density reaches a local maximum along the mantle interface, where the vanishing of the axial velocity causes the remaining velocity components (u_r and u_θ) as well as the vorticity vector to lie within the same r-θ plane.

Despite the helical nature of this motion and its rotation about the $z-$axis, the absence of axial vorticity may be ascribed to the irrotational nature of the tangential velocity, which drives the evolution of the mean flow vorticity in the r-z plane. In fact, the present solution may be viewed as the combination of a non-swirling complex-lamellar flowfield (with $\mathcal{H} = 0$) and an irrotational vortex exhibiting a tangential velocity that is solely responsible for the axially revolving motion. In this case, the generation of vorticity can be directly linked to the axial and radial velocity gradients, which are inherent to the bidirectional vortex motion, and not to the shearing process *per se*.

Before leaving this section, it may be helpful to clarify that a generalized Beltramian motion of this type has also been referred to in the literature as being quasi complex lamellar,[11,12,38] and this may be attributed to its incorporation of most essential characteristics of a complex-lamellar field. Since the axial and radial velocities are deduced from a stream function formulation of Euler's momentum equation, namely, the BHE transformation, one may realize that the tangential velocity is imposed rather separately in a manner to keep u_θ decoupled from the stream function. When examining the resulting model from this perspective, it can be seen that the complex-lamellar profile prescribed by the stream function is simply rotated about the central axis at an angular speed that is prescribed by the irrotational tangential velocity. It then becomes a simple exercise to verify that the two-component (u_r, u_z) motion established in the r-z plane satisfies the complex-lamellar criterion of $\mathbf{u} \cdot \boldsymbol{\omega} = 0$, thus justifying the naming attribution attached to this particular solution.

V. CONCLUSIONS

In this work, an exact incompressible solution is developed in the context of an inviscid bidirectional vortex in a right-cylindrical chamber with a hollow core. The presence of a hollow core may be instigated by a variety of factors that include the presence of a vortex finder or a tubular insert in industrial systems; it may be also caused by the onset of flow stratification or air entrapment within the core region of certain chemical and propulsive devices. Although the present analysis extends former work by Vyas and Majdalani,[38] the approach that we pursue begins with the Bragg–Hawthorne equation as opposed to the vorticity transport equation used previously. Nonetheless, regardless of the road taken, the same governing equation is recovered under the proper assumptions for B and H given by Eqs. (2) and (3). Another distinguishing feature that may be worth mentioning is that the present flowfield proves to be of the generalized Beltramian type and, by virtue of its ability to incorporate a hollow core internally, it may be viewed as a generalization of the analogous problem with no hollow core. It should be further noted that, in seeking a simple outcome, only one partial solution satisfying the problem's solvability condition is considered here, thus leading to the most compact expression that is still capable of securing the problem's fundamental constraints. In future work, a broader formulation may be pursued by summing up all viable eigen solutions in a linear superposition that aims at extending the model's applicability to more elaborate inlet and outlet boundary conditions.

In the presence of a hollow core, our findings indicate that the peak axial velocity will invariably increase with successive expansions of the core radius, namely, in observance of mass conservation. By the same token, the peak radial velocity will diminish with incremental reductions in the radial distance between the core boundary and the sidewall. Furthermore, the mantle, which proves to be a defining property of bidirectional fields, is shown to possess a simple dependence on the non-dimensional core radius α. Accordingly, the projected flow areas of the inner and outer swirling regions remain equally divided by the mantle interface even with a changing core diameter. As for the tangential velocity, its inviscid form proves to be consistent with that of an irrotational vortex.[38] In the present formulation, however, u_θ remains finite so long as $\alpha > 0$ over a discrete range of $r \in [\alpha, 1]$. As for the pressure, it is confirmed that variations in the hollow core diameter have minimal impact on Δp, and that visible deviations will only occur at high aspect ratios and impractically large values of the inflow parameter κ. Finally, and consistently with previous formulations, the radial and axial components of vorticity are seen to vanish identically, while leaving only one azimuthal term whose peak vorticity magnitude is realized in the outer vortex region irrespectively of α.

Having arrived at a compact representation of the bidirectional vortex with a hollow core in a frictionless environment, it is possible to extend the analysis by incorporating the effects of viscous boundary layers along the walls. The incumbent analysis will require the use of small perturbation techniques, such as matched-asymptotic expansions, to derive judicious approximations that are capable of satisfying the problem's velocity adherence requirements. Such work, along with similar treatment of the Beltramian flow analogue, will be the subject of forthcoming analysis.

ACKNOWLEDGMENTS

This work was supported partly by the National Science Foundation, through Grant No. CMMI–1761675, and partly by the Hugh and Loeda Francis Chair of Excellence, Department of Aerospace Engineering, Auburn University. The authors are deeply indebted to Martin J. Chiaverini, Director of Propulsion Systems at Sierra Space Corporation, and to Donald Benner, Brian Pomeroy, and Arthur Sauer, for numerous technical exchanges and for their unwavering support of the cyclonic flow investigations. We also thank Cody M. Shelton for his assistance in determining the asymptotic approximation for the peak vorticity location.

AUTHOR DECLARATIONS

Conflict of Interest

The authors have no conflict to disclose.

DATA AVAILABILITY

The data that support the findings of this study are available from the corresponding author upon reasonable request.

APPENDIX: CHARACTERISTICS OF THE PEAK RADIAL VELOCITY

As mentioned in Sec. IV B 2, closed-form expressions may be derived for the peak radial velocity and its location. First, the peak radial velocity may be approximated by

$$(u_r)_{\min} \approx -\frac{1.508\,786\kappa}{1 + 0.514\,711\alpha^2 - 0.228\,724\alpha^2 \ln \alpha}, \tag{A1}$$

where the denominator clearly grows with α. As α becomes larger than 0.3, the peak radial velocity becomes expressible through a linear relation of the form

$$(u_r)_{\min} \approx 1.589\,752 - 0.6\alpha. \tag{A2}$$

Along similar lines, the location of the peak radial velocity may be extracted from the transcendental root of Eq. (29); this may be approximated by

$$r_{\min} \approx 0.609\,106(1 + 0.641\,045\alpha^2 - 0.487\,191\alpha^2 \ln \alpha), \tag{A3}$$

over the full range of $\alpha \in [0, 1)$. For $\alpha > 0.3$, the behavior becomes so linear that it may be captured by

$$r_{\min} \approx 0.468\,248\alpha + 0.527\,029. \tag{A4}$$

In a similar manner, approximations for $x_{\min}$ can be obtained, specifically

$$x_{\min} \approx \frac{0.609\,106(1 + 0.338\,101\alpha + 0.549\,163\alpha^2 - 0.248\,789\alpha^3)}{1 + \alpha} \tag{A5}$$

along with a two-term expression in the linear range where

$$x_{\min} \approx 0.531\,081 - 0.031\,743\alpha, \quad \alpha > 0.6. \tag{A6}$$

REFERENCES

[1] W. H. Knuth, P. A. Bemowski, D. J. Gramer, J. Majdalani, and W. J. Rothbauer, "Gas-Fed, Vortex Injection Hybrid Rocket Engine," SBIR Phase I, NASA Final Technical Contract No. NAS8-40679 (Orbital Technologies Corporation, Madison, WI, 1996).

[2] M. J. Chiaverini, M. J. Malecki, A. Sauer, D. J. Gramer, W. H. Knuth, and J. Majdalani, "Vortex thrust chamber testing and analysis for O2-H2 propulsion applications," AIAA Paper No. 2003-4473, 2003.

[3] W. H. Knuth, M. J. Chiaverini, D. J. Gramer, and J. A. Sauer, "Final Report on Vortex Combustion Ramjet—A Phase I SBIR Project," SBIR Phase I, NASA Final Technical Contract No. NAS3-99039, OTC-GS075-FR-99-1 (Orbital Technologies Corporation, Madison, WI, 1999).

[4] M. J. Chiaverini, J. A. Sauer, and W. H. Knuth, "Final Report on Vortex Combustion combined Cycle Engine—A Phase I SBIR Project," AFRL Contract No. F04611-99-C-0063, OTC-GS082-FR-99-1 (Orbital Technologies Corporation, Madison, WI, 1999).

[5] M. J. Chiaverini, M. J. Malecki, J. A. Sauer, W. H. Knuth, and C. D. Hall, "Final Report on Cold-Wall Vortex Combustion Chamber—A Phase I SBIR Project," NASA Contact No. NAS8-01073 OTC-GS0107-01-1 (Orbital Technologies Corporation, Madison, WI, 2001).

[6] M. J. Chiaverini, M. J. Malecki, J. A. Sauer, and W. H. Knuth, "Vortex combustion chamber development for future liquid rocket engine applications," AIAA Paper No. 2002-4149, 2002.

[7] J. A. Sauer, W. H. Knuth, M. J. Malecki, M. J. Chiaverini, and C. D. Hall, "Development of a LOX/RP-1 vortex combustion cold-wall thrust chamber assembly," AIAA Paper No. 2002-4144, 2002.

[8] S. M. Munson, J. A. Sauer, J. D. Rocholl, and M. J. Chiaverini, "Development of a low-cost vortex-cooled thrust chamber using hybrid fabrication technique," AIAA Paper No. 2011-5835, 2011.

[9] J. Majdalani and M. J. Chiaverini, "Characterization of GO2–GH2 simulations of a miniature vortex combustion cold-wall chamber," J. Propul. Power **33**, 387–397 (2017).

[10] T. A. Barber and J. Majdalani, "On the Beltramian motion of the bidirectional vortex in a conical cyclone," J. Fluid Mech. **828**, 708–732 (2017).

[11] J. Majdalani, "Helical solutions of the bidirectional vortex in a cylindrical cyclone: Beltramian and Trkalian motions," Fluid Dyn. Res. **44**, 065506 (2012).

[12] L. L. Williams and J. Majdalani, "An exact irrotational solution for a hemispherically bounded cyclonic flowfield," Phys. Fluids **33**, 063608 (2021).

[13] J. Majdalani and L. L. Williams, "A quasi complex-lamellar solution for a hemispherically bounded cyclonic flowfield," Phys. Fluids **33**, 083105 (2021).

[14] L. L. Williams and J. Majdalani, "Exact Beltramian solutions for hemispherically bounded cyclonic flowfields," Phys. Fluids **33**, 093601 (2021).

[15] K.-Y. Hsu, L. P. Goss, and W. M. Roquemore, "Characteristics of a trapped-vortex combustor," J. Propul. Power **14**, 57–65 (1998).

[16] V. R. Katta and W. M. Roquemore, "Study on trapped-vortex combustor-effect of injection on flow dynamics," J. Propul. Power **14**, 273–281 (1998).

[17] M. D. Durbin, M. D. Vangsness, D. R. Ballal, and V. R. Katta, "Study of flame stability in a step-swirl combustor," J. Eng. Gas Turbines Power **118**, 308–314 (1996).

[18] V. Katta and W. Roquemore, "Numerical studies of trapped-vortex combustor," AIAA Paper No. 96-2660, 1996.

[19] I. Matveev, "Design and preliminary test results of the plasma assisted tornado combustor," AIAA Paper No. 2007-5628, 2007.

[20] I. Matveev, S. Matveeva, E. Kirchuk, and S. Serbin, "Experimental and theoretical investigations of a triple vortex combustor with spatial arc," AIAA Paper No. 2008-963, 2008.

[21] S. Long, T. C. W. Lau, A. Chinnici, Z. F. Tian, B. B. Dally, and G. J. Nathan, "Iso-thermal flow characteristics of rotationally symmetric jets generating a swirl within a cylindrical chamber," Phys. Fluids **30**, 055110 (2018).

[22] R. Gupta, M. D. Kaulaskar, V. Kumar, R. Sripriya, B. C. Meikap, and S. Chakraborty, "Studies on the understanding mechanism of air core and vortex formation in a hydrocyclone," Chem. Eng. J. **144**, 153–166 (2008).

[23] T. Neesse and J. Dueck, "Air core formation in the hydrocyclone," Miner. Eng. **20**, 349–354 (2007).

[24] G. Sharma and J. Majdalani, "Effects of nozzle inlet size and curvature on the flow development in a bidirectional vortex chamber," Phys. Fluids **33**, 093607 (2021).

[25] O. Khan, "An Experimental Investigation of Confined Cyclonic Flows and Ensuing Jet," Ph.D. dissertation (Auburn University, Department of Aerospace Engineering, Auburn, AL, 2021).

[26] M. R. Davidson, "An adaptive method of predicting the air core diameter for numerical models of hydrocyclone flow," Int. J. Miner. Process. **43**, 167–177 (1995).

[27] W. K. Evans, A. Suksangpanomrung, and A. F. Nowakowski, "The simulation of the flow within a hydrocyclone operating with an air core and with an inserted metal rod," Chem. Eng. J. **143**, 51–61 (2008).

[28] Q. A. Luo, C. L. Deng, J. R. Xu, L. X. Yu, and G. G. Xiong, "Comparison of the performance of water-sealed and commercial hydrocyclones," Int. J. Miner. Process. **25**, 297–310 (1989).

[29] S. J. Ying and C. C. Chang, "Exploratory model study of tornado-like vortex dynamics," J. Atmos. Sci. **27**, 3–14 (1970).

[30] M. I. G. Bloor and D. B. Ingham, "The flow in industrial cyclones," J. Fluid Mech. **178**, 507–519 (1987).

[31] M. R. Davidson, "Similarity solutions for flow in hydrocyclones," Chem. Eng. Sci. **43**, 1499–1505 (1988).

[32] S. V. Alekseenko, P. A. Kuibin, V. L. Okulov, and S. I. Shtork, "Helical vortices in swirl flow," J. Fluid Mech. **382**, 195–243 (1999).

[33]S. V. Alekseenko, P. A. Kuibin, and V. L. Okulov, *Theory of Concentrated Vortices: An Introduction* (Springer, Berlin, Germany, 2007).
[34]F. Concha, "Flow pattern in hydrocyclones," Kona Powder Part. **25**, 97–132 (2007).
[35]C. Cortes and A. Gil, "Modeling the gas and particle flow inside cyclone separators," Prog. Energy Combust. Sci. **33**, 409–452 (2007).
[36]V. N. Shtern and A. A. Borissov, "Nature of counterflow and circulation in vortex separators," Phys. Fluids **22**, 083601 (2010).
[37]F. Battaglia, R. G. Rehm, and H. R. Baum, "The fluid mechanics of fire whirls: An inviscid model," Phys. Fluids **12**, 2859–2867 (2000).
[38]A. B. Vyas and J. Majdalani, "Exact solution of the bidirectional vortex," AIAA J. **44**, 2208–2216 (2006).
[39]J. Horlock, *Actuator Disk Theory: Discontinuities in Thermo-Fluid Dynamics* (McGraw Hill, Inc., 1978).
[40]P. G. Saffman, *Vortex Dynamics*, Cambridge Monographs on Mechanics (Cambridge University Press, New York, 1992).
[41]G. K. Batchelor, *An Introduction to Fluid Dynamics* (Cambridge University Press, New York, 2000).
[42]P. J. Pritchard and J. W. Mitchell, *Fox and McDonald's Introduction to Fluid Mechanics*, 9th ed. (Wiley, Hoboken, NJ, 2015).
[43]J. D. Anderson, *Fundamentals of Aerodynamics*, 6th ed. (McGraw Hill, Princeton, NJ, 2017).
[44]H. Schlichting and K. Gersten, *Boundary-Layer Theory*, 9th ed. (Springer-Verlag, Berlin, 2017).
[45]F. M. White and J. Majdalani, *Viscous Fluid Flow*, 4th ed. (McGraw Hill, New York, 2021).
[46]W. M. Hicks, "II. Researches in vortex motion—Part III. On spiral or gyrostatic vortex aggregates," Philos. Trans. R. Soc. London, Ser. A **192**, 33–99 (1899).
[47]F. E. C. Culick, "Rotational axisymmetric mean flow and damping of acoustic waves in a solid propellant rocket," AIAA J. **4**, 1462–1464 (1966).
[48]A. B. Vyas, J. Majdalani, and M. J. Chiaverini, "The bidirectional vortex. Part III. Multiple solutions," AIAA Paper No. 2003-5054, 2003.
[49]J. Majdalani, "Unified framework for modeling swirl dominated helical motions," AIAA Paper No. 2014-3677, 2014.
[50]J. L. Smith, "An experimental study of the vortex in the cyclone separator," J. Basic Eng. **84**, 602–608 (1962).
[51]J. L. Smith, "An analysis of the vortex flow in the cyclone separator," J. Basic Eng. **84**, 609–618 (1962).
[52]H. K. Moffatt, "The degree of knottedness of tangled vortex lines," J. Fluid Mech. **35**, 117–129 (1969).